Fuel Processing Technology 215 (2021) 106755

Contents lists available at ScienceDirect

Fuel Processing Technology

journal homepage: www.elsevier.com/locate/fuproc

Research article

A simulation-based parametric study of CLOU chemical looping reactor performance

Zachary Reinking [a], Kevin J. Whitty [a], JoAnn S. Lighty [b,*]

[a] Department of Chemical Engineering, University of Utah, 50 S. Central Campus Drive, Room 3290, Salt Lake City, UT 84112, USA
[b] Department of Mechanical and Biomedical Engineering, Boise State University, 1910 University Dr., Boise, ID 83725, USA

ARTICLE INFO

Keywords:
Chemical looping
Computational fluid dynamics
Fluidized beds
Chemical looping with oxygen uncoupling
Multi-phase particle-in-cell method

ABSTRACT

Chemical looping with oxygen uncoupling (CLOU) is a variant on chemical looping combustion in which the oxygen carrier releases gaseous O_2 in the fuel reactor, making it well-suited for solid fuels, since the released gaseous O_2 readily reacts with solid char. This study presents several computational fluid dynamic (CFD) simulations of copper-based CLOU in a dual fluidized bed system, each with different operating conditions. The modeling predicted that coal particle sizes as large as 1000 μm did not significantly affect performance. Increased oxygen carrier copper loading resulted in an excess of gaseous oxygen in the product gas stream. Decreasing the oxygen carrier bed mass as well as reducing the air reactor fluidizing velocity did not supply enough oxygen to the fuel reactor to complete combustion of the coal. This generated a failure state in which the temperature continued to decrease in the fuel reactor from the lack of combustion, which in turn reduced the O_2 equilibrium partial pressure, further lowering the amount of combustion possible. Sufficient O_2 can be maintained in the fuel reactor by ensuring a high enough air reactor velocity and a large enough supply of oxygen carrier inventory to handle the chosen coal feed rate.

1. Introduction

There is significant interest in mitigating global climate change by controlling CO_2 emissions from fossil fuels. Chemical looping combustion (CLC) is a promising method for CO_2 capture during energy production [4,13,21]. CLC involves cycling metal-based "oxygen carrier" (OC) particles between two fluidized-bed reactors. The metal is oxidized in the air reactor (AR) and reduced in the fuel reactor (FR), where fuel is introduced and indirectly combusted by oxygen from the oxygen carrier. The separation of these two reactors prevents the mixing of air and fuel and effects in-situ air separation. Because of this, the fuel reactor produces a product gas containing mostly CO_2 that is free of nitrogen. Afterward, the oxygen carrier is returned to the AR to be re-oxidized.

In conventional CLC, when using solids fuels, there is an additional step in which the fuel must be gasified by CO_2 or steam to produce CO and H_2, which can then react with the lattice oxygen in the oxygen carrier. Chemical looping with oxygen uncoupling (CLOU), a variant of CLC, was developed to overcome challenges associated with slow gasification reactions [23,25]. In CLOU, a specific metal oxide is used that will spontaneously release gaseous oxygen (O_2) in the FR due to the low partial pressure of O_2 in that reactor. This allows for heterogeneous oxidation of solid fuels without gasification. Suitable CLOU oxides include CuO, Mn_2O_3, and Co_3O_4 ([1–3]; Mattisson et al., 2009) Amongst these. The CuO-Cu_2O pair has been shown to be particularly suitable for CLOU [10,22] due to its fast reaction times and oxygen release at typical combustion temperatures (950 °C). The copper cycles between cuprous (Cu_2O) and cupric (CuO) oxides per the reaction $Cu_2O + ½O_2 \leftrightarrow 2CuO$, with the forward reaction taking place in the air reactor and the reverse reaction taking place in the fuel reactor.

Simulation of fluidized beds using CFD can be used to aid reactor design and scale-up. Examples of approaches for fluidized bed modeling include the two-fluid model (TFM), discrete element method (DEM), and the multiphase-particle in cell (MP-PIC) method. The DEM and the MP-PIC method both use the Eulerian-Lagrangian (*E*-L) approach in which particles are Lagrangian computational particles and gas is treated as a continuum [28]. These kinds of methods have seen increased popularity with the recent advances in GPU speed.

The MP-PIC method is used by CPFD Software's Barracuda-VR™ gas-solid software, which is used as the basis for this study. MP-PIC is especially useful for simulating industrial-scale fluidized beds with high particle loading since the method uses particle clouds to limit the number of computational particles used. The original MP-PIC method is described in a publication by Andrews & O'Rourke [5], with more

* Corresponding author.
E-mail address: joannlighty@boisestate.edu (J.S. Lighty).

https://doi.org/10.1016/j.fuproc.2021.106755
Received 21 August 2020; Received in revised form 25 January 2021; Accepted 26 January 2021

Nomenclature

A_w	Wall area (m^2)
ϵ_p	Volume-weighted average of particle emissivity (–)
ϵ_w	Wall emissivity
ϵ_{wp}	Effective emissivity between wall and particle (–)
F_{wp}	View factor (–)
g	Acceleration from gravity (m^2/s)
h(T)	Enthalpy (J/kg)
k_i	Kinetic constant (atm/s)
P	Pressure (Pa)
P_i	Partial pressure of species i (atm)
$P_{i,\,e}$	Equilibrium partial pressure (atm)
ψ	Fraction of carbon content converted to CO_2 (–)
σ	Stefan-Boltzmann constant ($J/(m^2*s*K^4)$)
ρ_i	Density (Kg/m^3)
T	Temperature (K)
T_p	Mass-weighted average temperature of particles in a cell (K)
T_w	Wall temperature (K)
θ_f	Volume fraction of fluid (–)
θ_s	Volume fraction of solid (–)
$\theta_{s,\,cp}$	Volume fraction of solid at close-pack (–)
u	Velocity (m/s)
X	Fraction of fully oxidized copper (–)
X_i	Conversion of species i (–)
$Y_{f,\,i}$	Fluid mass fraction of species i (–)
x, y, z, u, v	Mols char for C, H, N, O, S (mols)

Table 1
Simulated cases.

	Base	Fuel Changes		Oxygen Carrier Changes		
		Fuel Input	Coal particle size	Inventory	Copper Loading	Alternate Carrier
Fuel input (kW_{th})	200	***50, 100, 150***	200	200	200	200
Avg coal particle size (μm)	150	150	***1000***	150	150	150
Total bed material inventory (kg)	200	200	200	***100, 150***	200	***90***
Oxygen carrier CuO loading (wt%)	20	20	20	20	***30***	***33***
Avg OC particle size (μm)	150 (100–200)	150 (100–200)	150 (100–200)	150 (100–200)	150 (100–200)	***360 (300–450)***
OC particle density (kg/m^3)	4100	4100	4100	4100	4100	***1300***

Table 2
Dimensions of PDU.

Component	FR	AR
Inner diameter	0.28 m	0.28 m
Height	5.7 m	6.0 m
Cyclone diameter	0.25 m	0.25 m
Cyclone inlet	0.10 m × 0.17 m	0.10 m × 0.17 m
Loop seal diameters	0.07 m	0.07 m

information in O'Rourke & Snider [26]. Previous simulations of CLC systems demonstrated the importance of 3D simulation [6]. Additional, recent simulations of CLC have also been done [8,14,15,18,20,24,34]. Barracuda-VR™ has also been used to simulate 3D CLC systems [9,17,27]. A 3D CLOU simulation of a 100 kW pilot-scale dual fluidized bed plant, incorporating chemical reactions and heat transfer, was performed by Reinking et al. [29].

In this study, we use simulation to explore different operating conditions for a 200 kW CLOU system. Fuel input, oxygen carrier characteristics, and hydrodynamic considerations were all investigated to develop a better understanding of operational performance.

2. Model development

The model simulates an existing chemical looping process development unit (PDU) that has two interconnected fluidized beds. Table 1 shows the different cases that were simulated. The base case represents a typical operating mode for the PDU. As noted above, three categories of changes were investigated: oxygen carrier changes, fuel changes, and changes in operating conditions.

2.1. Description of PDU

The PDU system that was simulated has two refractory-lined reactors with dimensions shown in Table 2. The air reactor (AR) is a single-pass circulating fluidized bed. Preheated air flows into the AR at a velocity of 5.0 m/s for the base case. Particles travel upwards with the fluidized gas and enter the AR cyclone, as shown by the arrows in Fig. 1. In the cyclone, they are separated from the now O_2 -depleted air and travel down a dipleg into the AR-FR loop seal, which is fluidized with air and steam. All material from the AR enters the FR. Because of this, the AR gas velocity correlates strongly with the solids circulation rate, and the AR gas velocity can be adjusted to change the overall oxygen carrier circulation rate.

Upon exiting the loop seal, particles flow into the bottom of the FR. The FR is a circulating fluidized bed. It is fluidized with superheated steam at 2.5 m/s in the base case. Commercial chemical looping systems will likely use recycled CO_2 to fluidize the FR reactor, but steam is used in the PDU because it is inexpensive and simple to produce. Particles flow up the FR to the FR cyclone, then down a dipleg into the fuel reactor recycle (FRR) loop seal, which is fluidized with steam. Recycling particles extends the residence time of the coal, which improves conversion. Particles in the FR are allowed to return to the AR via an overflow pipe that is 25% of the way up the FR, a distance of 1.45 m. A steam-fluidized loop seal connects the FR and AR.

Operating conditions used for the simulations are given in Table 3 and Table 4. Each reactor is fluidized at the bottom using a distributor. Coal is fed into the FR directly opposite of the FR-AR transfer loop seal near the bottom of the reactor. Loop seals are fluidized at two points, both pointing up in the z-direction. All loop seals are fluidized with steam except for the AR-FR loop seal fluidization port on the AR side of the loop seal. This port is fluidized with air to keep the oxygen carrier oxidized while still in the loop seal, though the other side of the loop seal is fluidized with steam in order to prevent most of that air from entering the FR. Nitrogen entering the FR would dilute the purity of exiting CO_2. Based on previous simulations, it was determined that N_2 leakage from the AR is negligible based on the amount of N_2 leaving the FR and the amount of nitrogen introduced via coal.

To allow control of reactor temperature in the simulation, a thermal

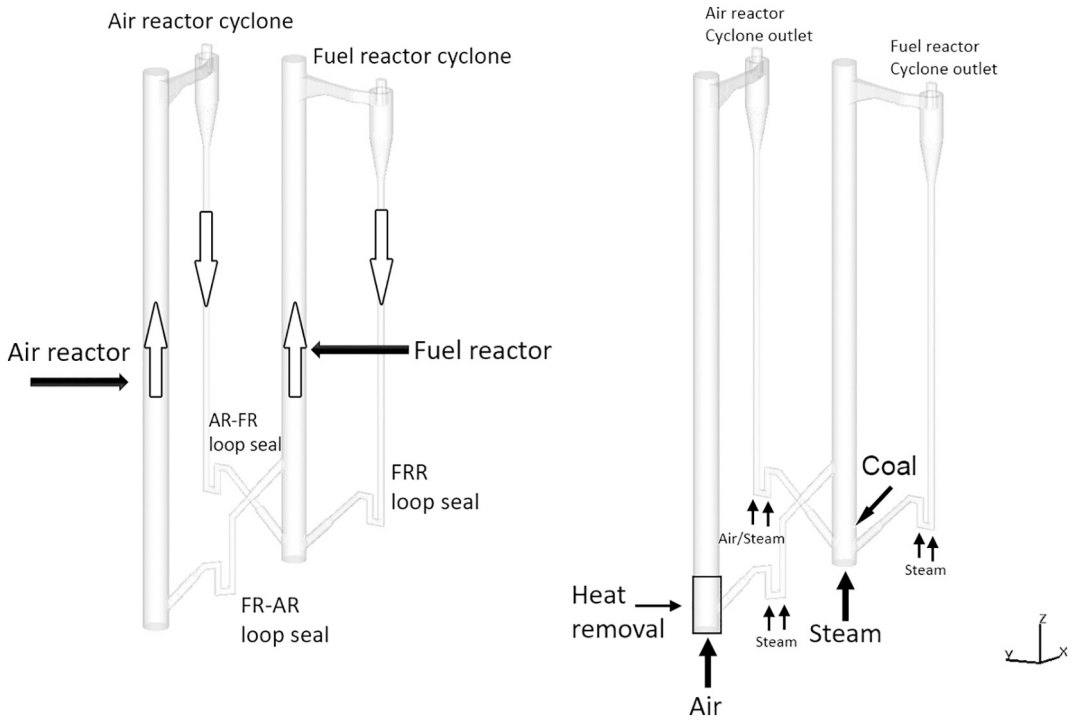

Fig. 1. Reactor configuration and location of boundary conditions.

Table 3
Base PDU fluidizing gas conditions.

Parameter	AR	FR
Fluidizing gas	Air	Steam
Gas temperature (°C)	900	700
Gas pressure (Pa, absolute)	87,000	87,000
Superficial velocity (m/s)	5.0	2.5

Table 4
PDU loop seal fluidizing gases.

Loop seal	Gas	Mass flow rate (kg/h)
AR to FR	Air and Steam	2.8, 2.8
FR to AR	Steam	0.5, 0.5
FR Recycle	Steam	5.0, 0.5

wall for heat removal was added to the bottom of the AR. The wall is 0.475 m in height and its surface temperature was set to 350 °C based on an estimated cooling water/steam temperature of 307 °C [12] and assuming an increasing temperature profile across the wall due to the high internal temperature of the reactor. A uniform boundary condition was used, assuming that the steam would be undergoing a phase transition and constant superheat temperature.

In the simulation, an extra boundary condition was added to recycle any material lost out of the FR and AR cyclones back into the corresponding loop seal. The particles were recycled in the exact state they left the cyclone, and no gas was recycled. This was done to keep the inventory constant between all cases throughout the entire simulation time.

2.2. Coal and oxygen carrier properties

Properties of the coal and oxygen carrier for each of the cases are given in Table 1. The oxygen carrier used was copper oxide on inert support with a given mass loading per case. Two types of support material were considered, a relatively dense but low porosity material and an alternative high-porosity, low-density engineered support. Sphericity was determined from experimental measurements and was 0.85 and 0.99 for the base case and alternative carrier, respectively. Sphericity is used in fluid-to-particle heat transfer calculations to determine surface area. The change in inventory for the two different carriers was initially based on reaching an equivalent amount of volume. Equivalent volume was used as the metric to determine the necessary amount of mass needed. However, it was determined that this amount of material, even with a very high copper oxide loading, would not be capable of circulating sufficient amounts of oxygen. Because of this, an equivalent volume was found and then was increased until this case had the same amount of copper oxide mass as the reduced inventory cases (30 kg).

Two coal sizes were considered, a smaller coal with a particle size range of 63–210 with an average size of 150 μm. The larger coal had a range of 900–1100, with an average size of 1000 μm. Particle density was 1100 kg m^{-3} for both cases, and sphericity was assumed to be 0.7.

The close pack solid volume fraction was taken from lab-scale characterization of actual carriers and was 0.63 for all particles used. Coal properties were based on typical values for Wyoming Powder River Basin (PRB) coal from the Black Thunder mine. This fuel was used because its ash has a low risk of agglomeration compared to other coal types in CLOU systems using copper oxide [11].

2.3. Barracuda-VR™ modeling

The hydrodynamic and heat transfer models have been previously described in Reinking et al. [29]. The hydrodynamic model was validated on a scaled-down, cold-flow version of the PDU, as seen in Hamilton et al. [16]. The drag model used was a correction for the Wen-Yu/Ergun blend using the Sauter Mean Diameter developed by Beetstra et al. [7]. Large-eddy simulation was used for turbulence modeling via the Smagorinsky subgrid-scale model (Smagorinsky [31]). A brief overview of the governing equations are as follows:

The fluid-phase momentum equations are:

$$\frac{\partial(\theta_f \rho_f)}{\partial t} + \nabla\cdot(\theta_f \rho_f \mathbf{u_f}) = \delta\dot{m}_p \quad (1)$$

$$\frac{\partial(\theta_f \rho_f \mathbf{u_f})}{\partial t} + \nabla\cdot(\theta_f \rho_f \mathbf{u_f}\mathbf{u_f}) = -\nabla P - \mathbf{F} + \theta_f \rho_f \mathbf{g} + \nabla\cdot(\theta_f \boldsymbol{\tau_f}) \quad (2)$$

θ_f is the volume fraction of the fluid, ρ_f is the density of the fluid, $\boldsymbol{u_f}$ is velocity, $\boldsymbol{\tau_f}$ is the fluid stress tensor, $\boldsymbol{g}$ is the gravitational acceleration, t is time and **F** is the rate of momentum exchange between the solid and fluid phase. $\delta\dot{m}_p$ is the fluid-mass source term determined from gas production from solid-gas chemistry.

Transport equations are solved for each gas species. Based on this fluid phase properties are determined from the mass fractions $Y_{f,\ i}$ of each gas species forming the mixture. Mass transferred through reaction by the chemical source term $\delta\dot{m}_{i,chem}$.

$$\frac{\partial(\theta_f \rho_f Y_{f,i})}{\partial t} + \nabla\cdot(\theta_f \rho_f Y_{f,i} \mathbf{u_f}) = \nabla\cdot(\rho_f D \theta_f \theta_f \nabla Y_{f,i}) + \delta\dot{m}_{i,chem} \quad (3)$$

D is the turbulent mass diffusivity which is based on the Schmidt number.

The fluid phase enthalpy equation is as follows:

$$\frac{\partial(\theta_f \rho_f h_f)}{\partial t} + \nabla\cdot(\theta_f \rho_f h_f \mathbf{u_f}) = \theta_f\left(\frac{\partial p}{\partial t} + \boldsymbol{u_f}\cdot\nabla p\right) - \nabla\cdot(\theta_f \boldsymbol{q}) + S_h + \dot{q}_D \quad (4)$$

Where h_f is fluid enthalpy, p is pressure, S_h is the conservative energy exchange from particle to fluid phase, and $\dot{q}_D$ is the enthalpy diffusion term.

The particle phase is predicted by solving a transport equation for the particle distribution function *f*. The particle distribution function is a function of particle position, velocity, mass, temperature and also time. The particle distribution function is not given explicitly in this work but can be found in Snider and O'Rourke (1996).

Particle-to-particle collisions in Barracuda are modeled by the particle normal stress:

$$\tau_s = \frac{10 P_s \theta_s^{\beta}}{max\left(\left(\theta_{s,cp} - \theta_s\right), \epsilon(1-\theta_s)\right)} \quad (5)$$

θ_s is the solid volume fraction and P_s is a pressure constant set to 15 with units of Pa. β is set to 3, and ϵ is set to a small number to avoid the singularity that happens when particles reach close-pack. $\theta_{s,\ cp}$ is the close-pack volume fraction. When the particle normal stress is high, collisions are frequent and the velocity increases, as a particle moves away from a packed area, collisions decrease. Particle velocity is the sum of the the particle velocity from normal stress, and from all other forceds. The particle normal stress is applied to a solid only up to the point where the solid reaches the particle-mean velocity.

A significantly more detailed explanation of modeling can be found in Snider [32] and Snider et al. [33]. This explicitly shows source terms, the momentrum transfer rate, particle volume fraction, particle acceleration, etc.

2.3.1. Chemical reactions

In order to keep simulation times low, a limited number of reactions were included. The principal reactions of importance were copper oxidation and reduction, as well as coal char oxidation. Other reactions, such as steam and CO_2 gasification, are slow compared to char oxidation, though these are also included along with homogenous oxidation reactions. A full summary of the reactions has been presented in Reinking et al. [29]. Production of nitrogen oxides was ignored as well as any potential interactions between species in the coal ash and the copper oxide itself.

CLOU copper oxide reaction kinetics were based on work by Clayton et al. [10] and Sahir et al. [30], who developed kinetics using Arrhenius and power-law expressions. These were later adapted into Barracuda-VR™ by Hamilton et al. [17] after slight modification. Additionally, it was shown that the metal-oxide reaction is not rate-limited by gas-phase mass transfer. The reactions are shown below, in addition to an approximation for partial pressure of oxygen as a function of temperature.

Table 5
Coal composition (as received).

Material	Mass fraction
Ash	0.049
Carbon Char	0.145
Hydrogen Char	0.151
Nitrogen Char	0.007
Oxygen Char	0.039
Sulfur Char	0.001
Moisture	0.182
Volatiles	0.426

$$\text{Reduction } \frac{dX_{CuO}}{dt} = k_{CuO}\left(P_{O_2,e} - P_{O_2}\right)(1 - X_{CuO}) \quad (6)$$

$$\text{Oxidation } \frac{dX_{Cu_2O}}{dt} = k_{Cu_2O}\left(P_{O_2}^{1.3} - P_{O_2 e}^{1.3}\right)(1 - X_{Cu_2O}) \quad (7)$$

$$P_{O_2,e} = 5.4{*}10^7 exp\left(-\frac{25600}{T}\right) \quad (8)$$

X represents the conversion of either cupric or cuprous oxide. P_{O2e} and $P_{O2}$are the equilibrium and actual partial pressures of oxygen. *k* is the kinetic constant determined from the Arrhenius equation and are shown below. T is temperature and is determined via a weighting of fluid and particle temperatures in the cell. The weighting is at 50:50 for both fluids and particles, and uses the average temperature of particles in the cell. R is the gas constant.

$$k_{CuO} = 3e^{-\frac{20000}{RT}} \quad (9)$$

$$k_{Cu_2O} = 56000e^{-\frac{68000}{RT}} \quad (10)$$

Enthalpy for CuO and Cu_2O are as follows:

$$Cu_2O h(T) = -1165000 - \int_{T_{ref}}^{T} 370 + 0.36T - 0.0003T^2 + 10^{-7}T^3 dT \quad (11)$$

$$CuO\ h(T) = -1951100 - \int_{T_{ref}}^{T} 526 + 0.22T - 5x10^{-5}T^2 dT \quad (12)$$

Where h(T) is in units of J/kg.

Oxidation of char ($C_xH_yN_zO_uS_v$) was expressed as:

$$C_xH_yN_zO_uS_v + \left(\frac{1+\psi}{2}x + \frac{1}{4}y + v - \frac{1}{2}u\right)O_2 \overset{overall}{\rightarrow} x\psi\ CO_2 + x(1-\psi)\ CO + \frac{1}{2}y\ H_2O + \frac{1}{2}z\ N_2 + v\ SO_2 \quad (13)$$

Where ψ is the fraction of carbon converted to CO_2 in a particle. A more significant discussion of how the reaction kinetics for char oxidation and other gas-solid reactions were implemented into the model can be found in previous work [29]. This paper uses an updated, more realistic steam

Table 6
Composition of volatiles released from coal.

Species	Volatile mass fraction
Methane	0.051
Carbon monoxide	0.329
Hydrogen gas	0.030
Other carbon	0.590

Table 7
Resulting values for different fuel input cases.

Case	Mass distribution (kg)			AR → FR Circulation (kg/s)	FRR circulation (kg/s)	Coal mass (kg)	AR residence time (s)	FR residence time (s)
	AR	FR	Loop seal & cyclone					
Base, 200 kW	4.4% (8.8)	62.9% (125.8)	32.7% (65.4)	0.88	1.47	0.00151	10	143
150 kW	3.3% (6.6)	64.6% (129.2)	32.1% (64.2)	0.78	1.46	0.00147	8	163
100 kW	3.4% (6.8)	65.0% (130.0)	31.6% (63.2)	0.80	0.91	0.00148	9	162
50 kW	3.0% (6.0)	67% (134.0)	30.0% (60.0)	0.75	0.62	0.00101	8	179
200 kW of 1000 μm coal	3.2% (6.4)	63.8% (127.6)	33.0% (66.0)	0.77	1.21	0.00160	10	167

gasification rate (roughly double that of the CO_2 rate), although values in the literature tend to vary depending on conditions [19].

The composition of gases released from the coal during devolatilization was estimated from the PRB coal composition, as seen in Table 5 and Table 6. 18% of the coal mass was moisture, and 43% was volatiles. Several species that would typically exist in volatiles, such as ammonia or hydrogen cyanide, were not included to preserve computational speed and memory.

The reaction rates of devolatilization, the evaporation rate, and the reaction coefficients were taken from Parker [27].

2.3.2. Thermal wall heat transfer

Barracuda-VR™ uses a radiation model that calculates radiative heat transfer between particles and the thermal wall. The model does not consider radiative heat transfer between wall and fluid, between particles, or between walls. The radiative heat transfer is calculated as follows:

$$q_{wp} = A_w F_{wp} \epsilon_{wp} \sigma \left(T_w^4 - \overline{T}_p^4 \right) \tag{14}$$

Where A_w is the thermal wall area, T_w the wall temperature, $\overline{T}_p$ the mass-weighted average of particles in a cell near the wall, F_{wp} is the view factor, σ the Stefan-Boltzmann constant, and $\epsilon_{wp}$is the effective emissivity between the particles in a cell and the thermal wall. Emissivity is determined by the following:

$$\epsilon_{wp} = \left(\frac{1}{\overline{\epsilon}_p} + \frac{1}{\epsilon_w} - 1 \right)^{-1} \tag{15}$$

For the calculation of emissivity, $\overline{\epsilon}_p$ is the volume-weighted average of particle emissivity's and ϵ_w is the emissivity of the wall. In order to keep the view factor calculation computationally fast, Barracuda only looks at cells near the wall and calculates the view factor based on the particle volume fraction, particle diameters, and local geometry.

Barracuda also determines convective fluid-to-wall heat transfer and

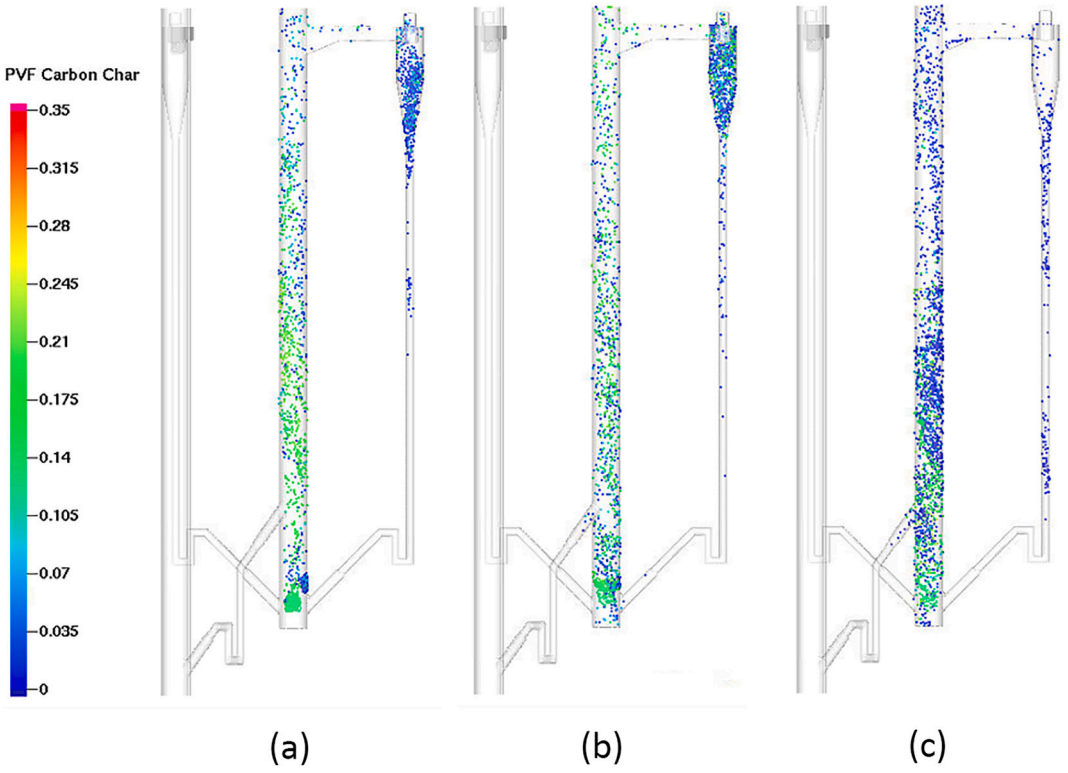

Fig. 2. Particle volume fraction of the carbon portion of char for (a) base case (200 kW), (b) lower fuel input case (100 kW), and (c) the larger coal size case, 1000 μm coal.

Table 8
Other values for changes to fuel input.

	AR Temperature top, bottom (°C)	FR Temperature top, bottom (°C)	*X* AR cyclone	*X* FR cyclone	Change in *X*	O_2 mol fraction at cyclone exit AR, FR	CO_2 mol fraction at cyclone exit AR, FR	Heat removal (kW)
Base, 200 kW	959, 929	968, 955	0.84	0.29	0.55	0.11, 0.045	1.1×10^{-5}, 0.14	60
150 kW	944, 909	954, 942	0.88	0.47	0.41	0.14, 0.035	4.5×10^{-6}, 0.11	53
100 kW	928, 900	939, 927	0.94	0.56	0.38	0.15, 0.030	4.9×10^{-6}, 0.080	50
50 kW	905, 881	917, 909	0.98	0.69	0.28	0.16, 0.025	2.0×10^{-6}, 0.044	45
1000 μm coal	970, 929	971, 961	0.81	0.21	0.60	0.12, 0.056	6.5×10^{-6}, 0.14	50

Table 9
Hydrodynamic values for base and reduced inventory cases.

	Mass distribution (kg)			AR → FR Circulation (kg/s)	FRR circulation (kg/s)	Coal mass (kg)	AR residence time (s)	FR residence time (s)
	AR mass	FR mass	Loop seal & cyclone mass					
Base (200 kg)	4.4% (8.8)	62.9% (125.8)	32.7% (65.4)	0.88	1.5	0.00151	10	143
150 kg	12.4% (18.6)	55.9% (83.9)	31.7% (47.5)	1.3	2.8	0.00457	14	65
100 kg	17.0% (17.0)	44.5% (44.5)	38.5% (38.5)	1.77	0.1	0.0271	10	25

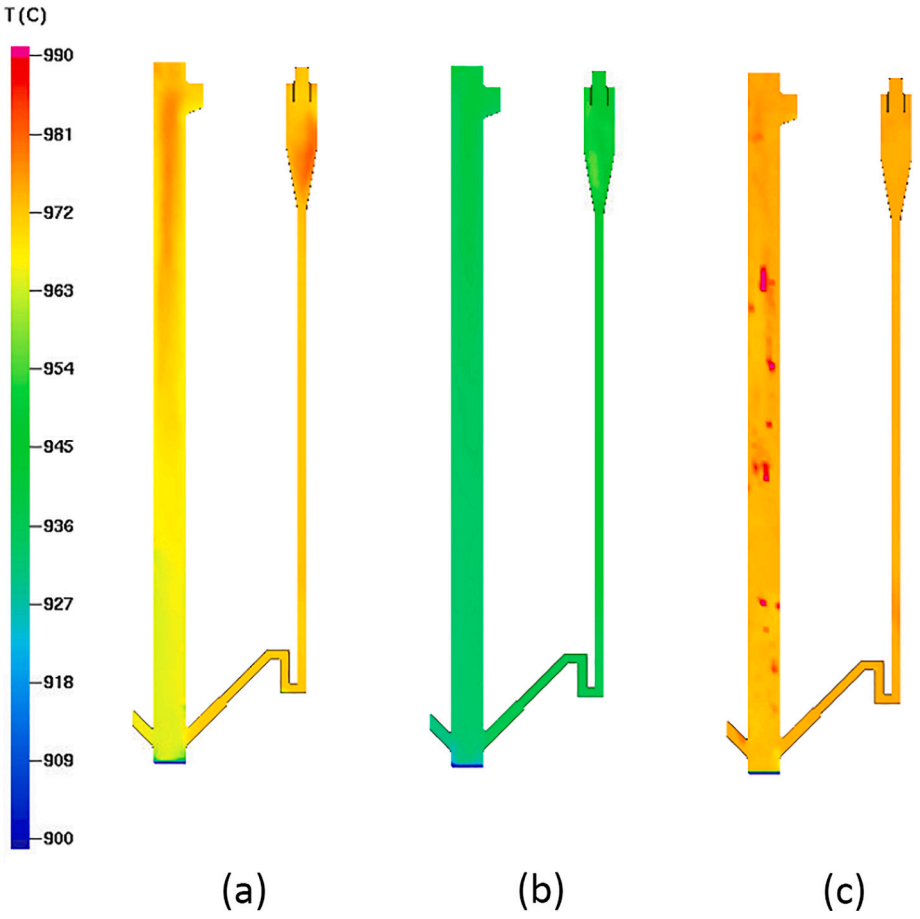

Fig. 3. Time-averaged fluid temperature for a cross-section of the FR for (a) base case, (b) lower fuel input case (100 kW), and (c) the larger coal size case.

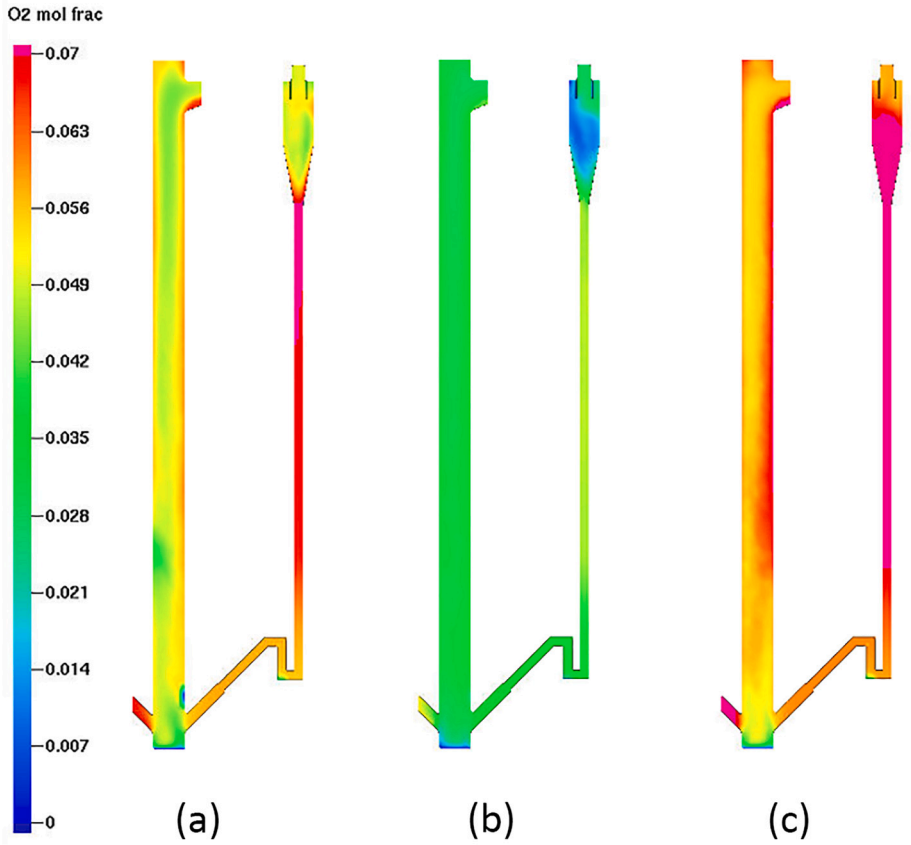

Fig. 4. Time-averaged O_2 mol fraction for a cross-section of the FR for (a) base case, (b) lower fuel input case (100 kW), and (c) the larger coal size case.

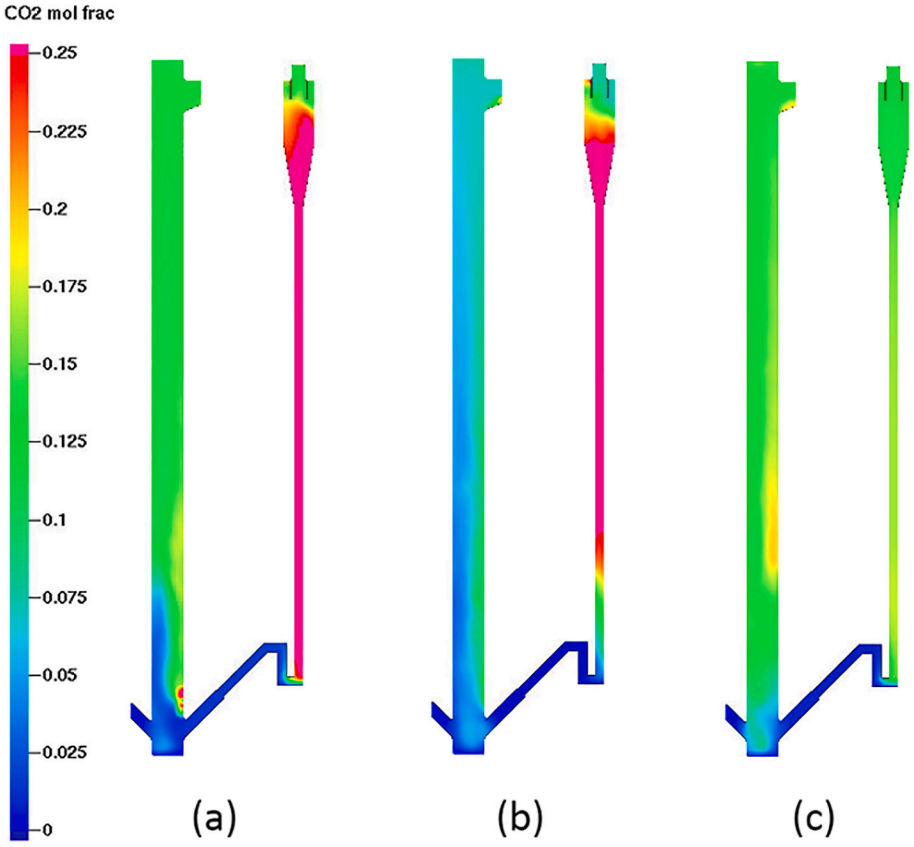

Fig. 5. Time-averaged CO_2 mol fraction for a cross-section of the FR for (a) base case, (b) lower fuel input case (100 kW), and (c) the larger coal size case.

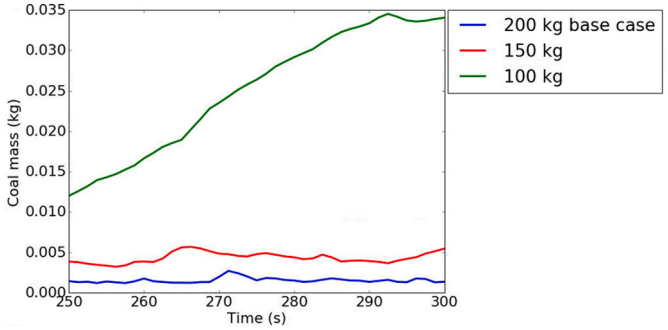

Fig. 6. Overall system coal mass (kg) vs. time (s) for the base (200 kg), 150 kg, and 100 kg inventory cases.

is based on Yang [35].

3. Results and discussion

Each simulation's grid was initialized with 1.5×10^6 cells, which resulted in roughly 100,000 real cells. The number of particles initialized was 3.3×10^{10}, which resulted in 400,000 particle clouds. The number of particles initialized was proportional to the mass inventory and, therefore, was lower for some simulations. No significant impact was found when the simulations were run at higher resolutions.

At the start of the simulation, both beds were slumped (no fluidizing gas was flowing). Oxygen carrier was initially distributed as 37.5% in the AR, 51.3% in the FR, and the rest distributed through the loop seals. More oxygen carrier was initially in the FR since its lower fluidizing velocity would yield a denser bed with more mass. Each simulation was run for 300 s of simulated physical time, which allowed each case to reach a hydrodynamic steady-state (inventory, circulation rate, etc.) and temperature changes of no more than 2–3 °C per minute. This is with the exception of two cases which "failed" due to not providing enough O_2 to the FR and had increasing coal-mass. The GPU used for each case was a GeForce GTX TITAN X (4600 cores). Simulations took 350–500 h to finish (wall-clock time), depending on the initial conditions.

Although it would be desirable to simulate a wide range of reactor sizes and designs, this is infeasible considering the computational time taken to complete each simulation. Currently, there is a very limited number of chemical looping systems of reasonable scale in the world. The design of the pilot system in this study is considered representative of how industrial-scale reactors will be configured, as most designs in the literature today involve two interconnected fluidized beds.

The motivation behind this study was to guide design and opearation of the PDU system being simulated, which is a complex and challenging system to operate in CLOU mode. One can ask whether there is more value in (1) simulating an existing, operating system that is well characterized but not easily modified based on simulation results, or (2) a not-yet-constructed system that can still be refined before it is constructed. While we agree that information on actual system performance is important and valuable, the trend in simulation science is to use such modeling as a tool for technology development; the latter was the goal of this study. The submodels for hydrodynamics, chemistry and heat transfer that form the basis for the simulation have been previously validated.

3.1. Influence of fuel changes

As shown in Table 1, the fuel changes included a change of fuel input (from 200 kW_{th} to 50 kW_{th}) and fuel size (from 150 μm to 1000 μm). The resulting masses of material and coal in each reactor and the diplegs was evaluated. Reactor mass was determined by summing the mass of each particle in the volume of each reactor. Coal mass was determined by multiplying the mass of particles in a cell by the volume fraction of coal in the cell for the entire system. The various circulation rates were determined by flux planes located in the dipleg of the AR and FR cyclones. The AR-FR circulation rate was an average of the material entering from the FR as well as leaving the AR. The residence time was determined by reactor mass and circulation rate. Each of these values was averaged over the last 50 s of simulation time.

Initially, a 300 kW case was also attempted. However, the system quickly became flooded with coal and could not keep up with the rate of fuel input. Because of this, this simulation did not complete and it is not included in this paper.

As seen in Table 7, only small differences in operation were observed when the fuel input rate changed. As predicted, most of the mass was in the FR due to the high velocity in the AR. The mass of unreacted coal did not significantly vary between the 200, 150, and 100 kW cases but was noticeably lower in the 50 kW case. Ash was not included in this summation, and ash content was proportional to the coal feeding rate and independent of conversion. Note that coal conversion exceeded 99% in all three cases.

Fig. 2 shows the particle volume fraction of carbon char for each case. The base case and lower fuel input cases are very similar, which agrees with the coal mass being the same between them. The case with a larger coal size notably had less coal in the cyclone than the other two cases. This was due to the coal being heavier because of its larger size. In the base case, the fine coal char is not easily separated and tends to "float" in the cyclone. With the larger sized coal, the char quickly enters the return dipleg. While there was a concern that there may be more unburnt char transporting to the AR, this was found not to be the case.

There was also a small observable trend of AR mass decreasing with decreasing fuel input rate (along with FR residence time increasing). This is likely due to a decrease in temperature in the FR in these cases, lowering the pressure in that reactor, and decreasing the ability to transport solids to the AR.

It is useful to know the fraction of copper oxide that is fully oxidized (CuO), defined as X:

$$X = \frac{mols\ CuO}{mols\ CuO + 2{*}mols\ Cu_2O} \tag{16}$$

One would expect X to be high at the exit of the air reactor and lower at the exit of the fuel reactor. X was calculated in the AR and FR cyclones.

The reactor temperature was determined by averaging over a volume encompassing the bottom third or top third of the reactor. This was also time-averaged for the last 50 s. Exit mol fractions were determined from flux planes located on the cyclone exits by converting mass fraction to mol fraction.

Table 10
Other values for base and reduced inventory cases.

	AR Temperature top, bottom (°C)	FR Temperature top, bottom (°C)	X AR cyclone	X FR cyclone	Change in X	O_2 mol fraction at cyclone exit AR, FR	CO_2 mol fraction at cyclone exit AR, FR	Heat removal (kW)
Base (200 kg)	959, 929	968, 955	0.84	0.29	0.55	0.110, 0.045	1.1×10^{-5}, 0.14	60
150 kg	969, 951	983, 966	0.55	0.07	0.48	0.077, 0.039	1.1×10^{-4}, 0.15	100
100 kg	964, 952	936, 934	0.57	0.09	0.48	0.044, 0.015	3.3×10^{-3}, 0.17	80

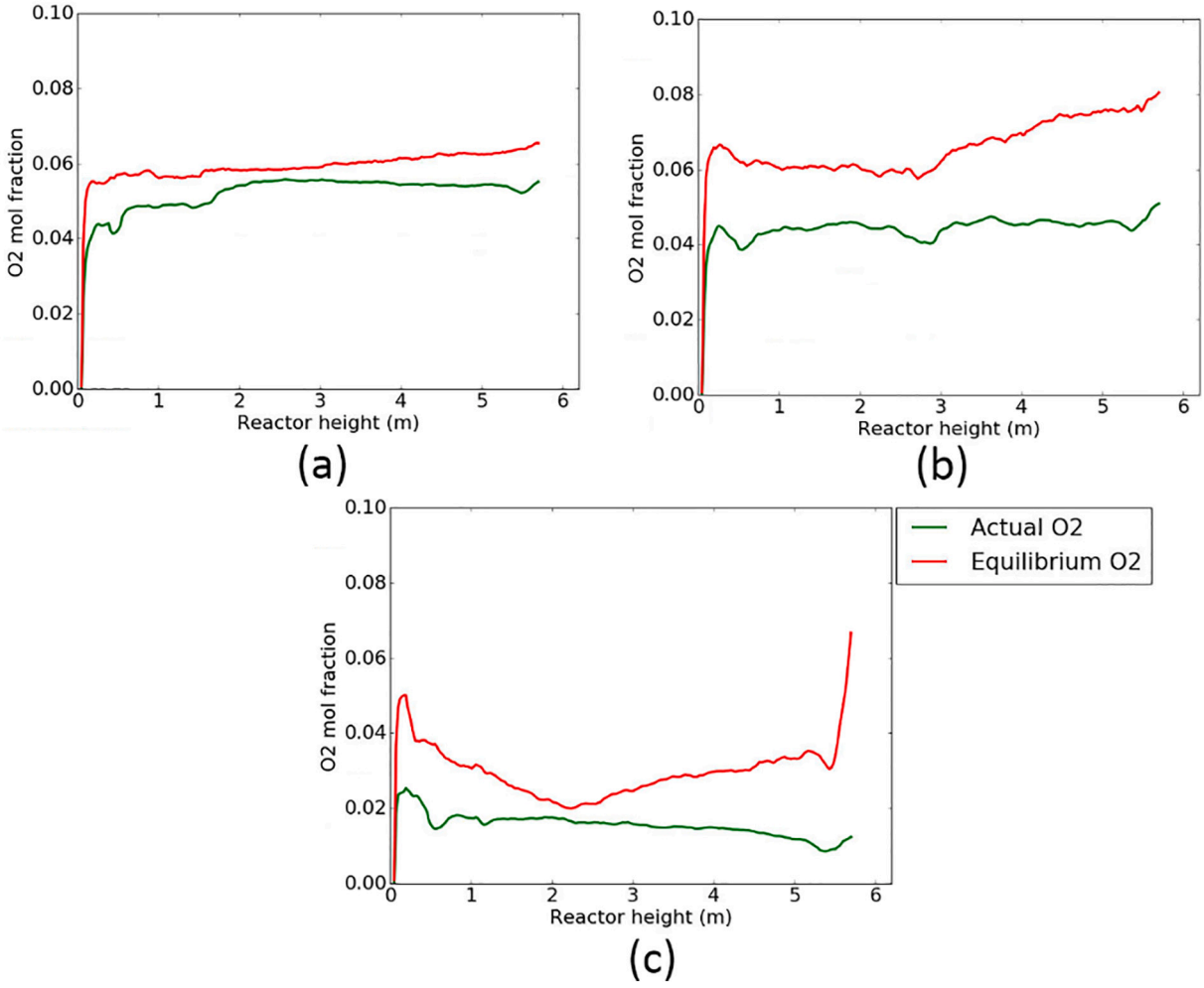

Fig. 7. O_2 mol fraction vs. FR reactor height (m) for (a) base (200 kg) (b) 150 kg inventory and (c) 100 kg inventory cases.

Table 11
Hydrodynamic values for base, alternate carrier, and increased copper loading cases.

	Mass distribution (kg)			AR → FR Circulation (kg/s)	FRR circulation (kg/s)	Coal mass (kg)	AR residence time (s)	FR residence time (s)
	AR mass	FR mass	Loop seal & cyclone mass					
Base	4.4% (8.8)	62.9% (125.8)	32.7% (65.4)	0.88	1.47	0.00151	10	143
Alternate carrier	20.4% (18.4)	50.9% (45.8)	28.7% (25.8)	0.86	1.13	0.00330	21	53
Increased copper loading	2.5% (5.0)	63.3% (126.6)	34.2% (68.4)	0.67	1.44	0.00095	8	188

Table 12
Other values for base, alternate carrier, and increased copper loading cases.

	AR Temperature top, bottom (°C)	FR Temperature top, bottom (°C)	*X* AR cyclone	*X* FR cyclone	Change in *X*	O_2 mol fraction at cyclone exit AR, FR	CO_2 mol fraction at cyclone exit AR, FR	Heat removal (kW)
Base	959, 929	968, 955	0.84	0.29	0.55	0.11, 0.045	1.1×10^{-5}, 0.14	60
Alternate carrier	955, 937	972, 959	0.71	0.22	0.49	0.07, 0.040	2.1×10^{-3}, 0.14	110
Increased copper loading	984, 928	977, 964	0.83	0.36	0.47	0.13, 0.063	1.5×10^{-7}, 0.14	50

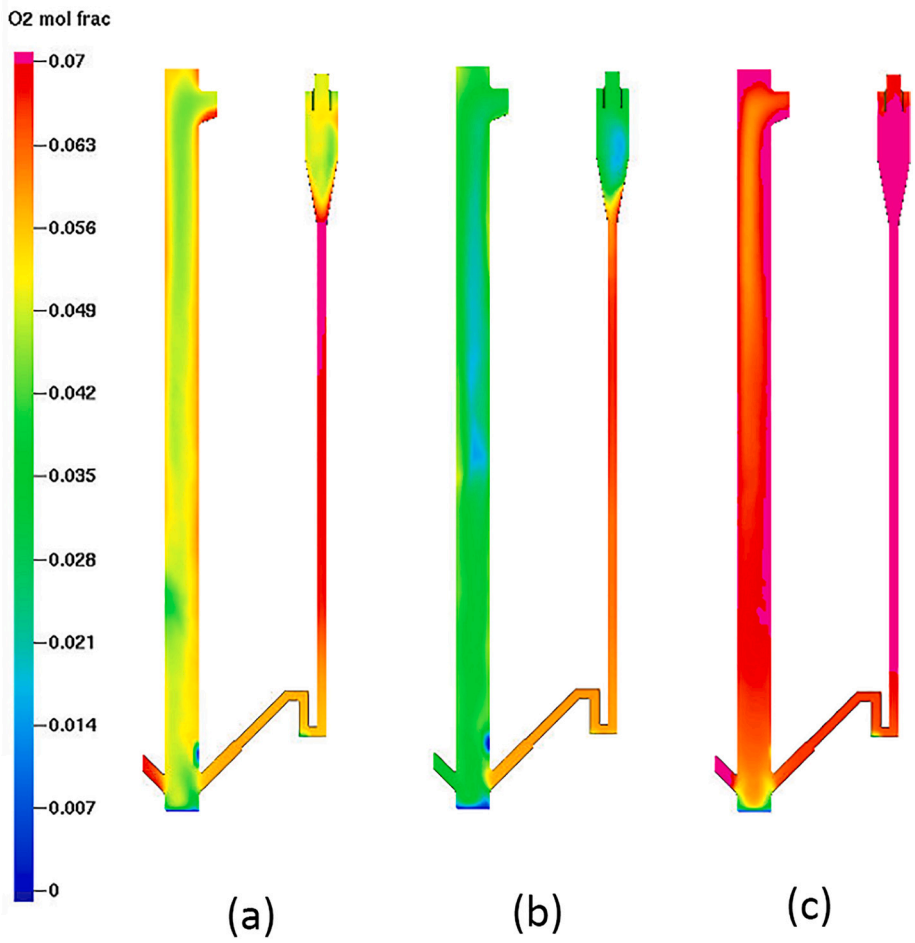

Fig. 8. Time-averaged O_2 mol fraction for a cross-section of the FR for (a) base, (b) alternate carrier, and (c) increased copper loading cases.

Table 8 summarizes conditions for the three cases. The temperatures were much lower for the lower fuel input case. This is a result of the reduced amount of fuel fed into the FR. This temperature difference might explain the result that the amount of unburned coal is nearly the same in each case, since the lower temperature of the low fuel input case results in slower fuel conversion. (See Table 9.)

The larger coal size case had slightly higher temperatures in the FR and AR than the base case, suggesting that fuel particle size has only a minor influence on reactor temperature over the ranges tested.

The change in X between the AR and FR cyclone was much lower for the lower fuel input cases than for the base case due to the lower oxygen requirement to combust the lower input of coal. Compared to the base case, the lower fuel input cases did not have as much O_2 in the FR cyclone exit. This is because those cases have a lower temperature in the FR, restricting the amount of O_2 that can be released. Temperature decreased with each iteration of lowering the fuel input rate. Note that when the O_2 partial pressure becomes equal to the partial pressure at equilibrium in the fuel reactor, the reaction driving force and the associated rate of reduction is zero. The reverse is also true of oxidation in the AR.

Cross-sections of the simulated reactor temperature for the FR in each case can be seen in Fig. 3. The temperature in the FR for the low fuel input case is notably lower than in the base case. Due to having more coal mass concentrated at the bottom of the reactor, the larger coal size case did not have a temperature spike in the cyclone like the base case did, as very little coal conversion was occurring in the cyclone for that case.

Fig. 4 shows the centerline O_2 mol fraction in the FR for each case. In all cases, the oxygen concentration in the FR was near equilibrium.

In the FR recycle dipleg, there was a noticeable spike of O_2 in all cases. The O_2 concentration in the FR recycle dipleg was consistently higher than in the fuel reactor due to a comparatively small amount of fuel available to consume O_2 released by the oxygen carrier. This also explains why in the larger coal size case, more O_2 is seen in the cyclone than the base case, as there is less coal entering the cyclone in that case due to its larger size and therefore mass per particle.

In Fig. 5, CO_2 concentrations in the FR can be seen for each case. The base case has significantly more CO_2 in the cyclone than in the larger coal size case, again signaling that there is a large amount of combustion occurring in the cyclone and loop seal. With large coal particles, the CO_2 is distributed more evenly over the height of the FR because the larger coal is heavier and spends more time in the bottom of the reactor. In the base case, there is little CO_2 at the bottom of the reactor. CO_2 is comparatively low in the reactor when the feed rate of coal is reduced.

Based on these results, it appears that the pilot plant could comfortably operate at a variety of different coal feeding rates lower than the base case. However, it does not appear that the unit would be able to operate at a 300 kW feeding rate.

3.2. Oxygen carrier changes

The oxygen carrier changes included using the same carrier with a higher copper concentration, as well as a different carrier, which was less dense but had a larger particle size, representing a carrier that would be manufactured using engineered catalyst support. Additionally, two cases were simulated in which there was a reduced oxygen carrier

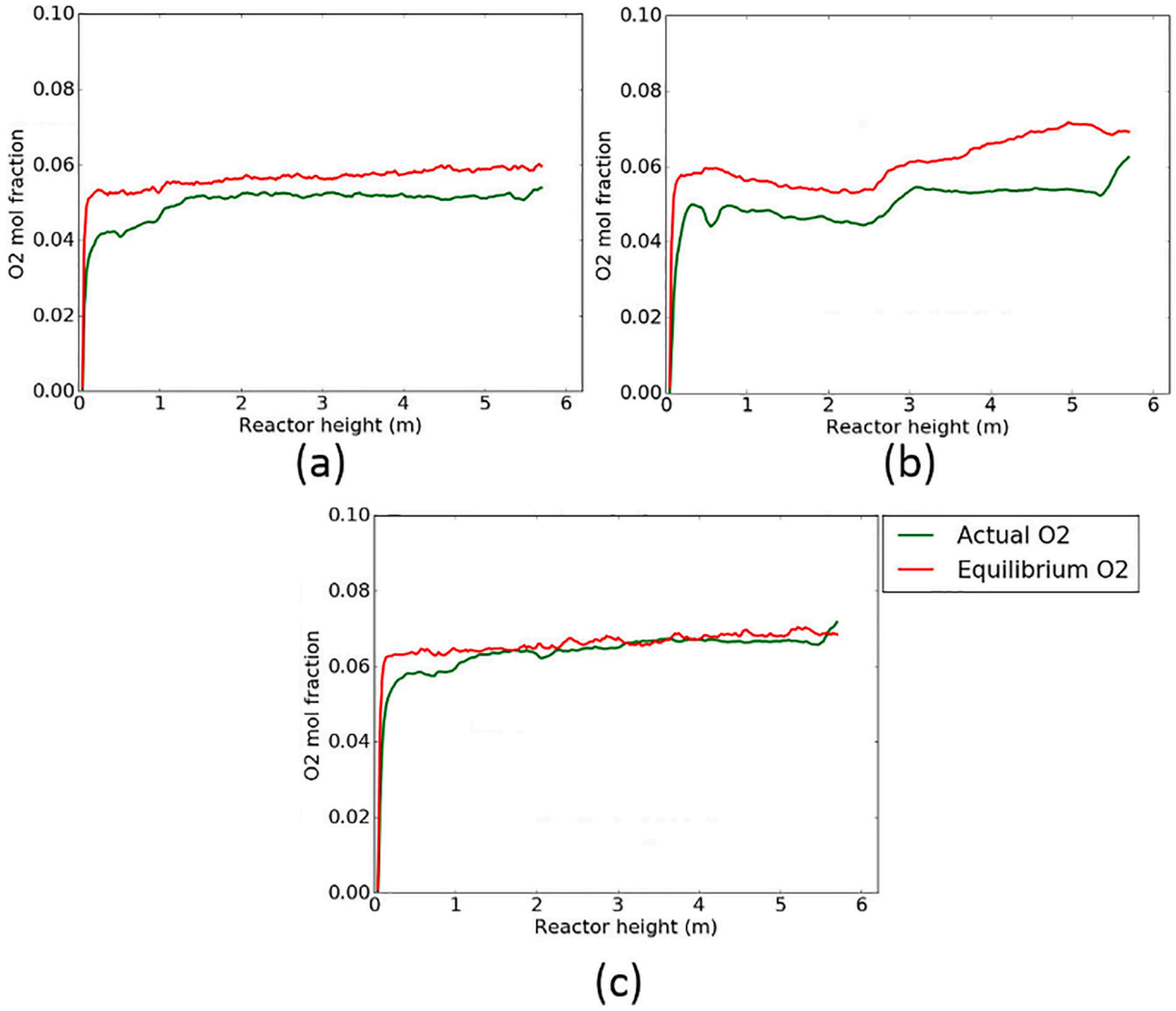

Fig. 9. O_2 mol fraction vs. FR reactor height (m) for (a) base, (b) alternate carrier, and (c) increased copper loading cases.

Table 13
Hydrodynamic values for base and various cases where fluidizing velocity is changed.

AR velocity (m/s)	FR velocity (m/s)	AR mass	FR mass	Loop seal and cyclone mass	AR → FR Circulation (kg/s)	FRR circulation (kg/s)	Coal mass (kg)	AR residence time (s)	FR residence time (s)
4.25	2.5	53.0%	19.8%	27.2%	1.71	1.1	0.0250	62	23
4.5		38.7%	38.6%	22.7%	0.75	2.70	0.0081	103	103
4.75		29.5%	40.0%	30.5%	1.00	1.46	0.0041	59	80
5.0		**4.4%**	**62.9%**	**32.7%**	**0.88**	**1.47**	**0.0015**	**10**	**143**
5.5		3.2%	63.0%	33.8%	0.91	1.56	0.0013	7	81
5.0	2.0	2.9%	65.2%	31.9%	0.74	0.86	0.0012	8	176
	4.0	24.9%	46.3%	22.8%	1.35	3.73	0.0036	37	69

inventory in the reactors instead of the base case at 200 kg.

3.2.1. Inventory

The most significant difference between the base and reduced inventory cases was in the circulation rate and inventory distribution. The AR had more mass when the inventory was lower (8.8 vs. 18.6 and 17.0 kg), and circulation from the AR to FR was higher. Unreacted coal mass was higher in the 150 kg inventory case and was significantly higher in the 100 kg case. Most likely, this is because of the decreased amount of oxygen the carrier was able to transport.

Notably, the FRR circulation rate in the 100 kg case was slow compared to the other cases. Pressure increased in the FR, forcing a large amount of inventory into the AR. The pressure increase also caused some backflow up the FRR loop seal.

The overall system coal mass was plotted for each case in Fig. 6. The coal transiently increased in the 100 kg inventory case. This is most likely a result of the lower amount of O_2 in the FR for this case, as well as the lower temperature due to the decreased amount of coal reacting.

Table 10 shows the differences in temperature, X, and O_2 mol fraction. Change in X was potentially lower in the reduced inventory cases due to the higher temperature in the AR, allowing the oxygen carrier to utilize more O_2 due to the corresponding decrease in equilibrium partial pressure. The temperature was higher in both reduced inventory cases due to the lower amount of inventory being unable to hold as much heat, resulting in an increase in gas temperature. The temperature in the 100 kg inventory case in the FR was notably much lower in the FR. This is

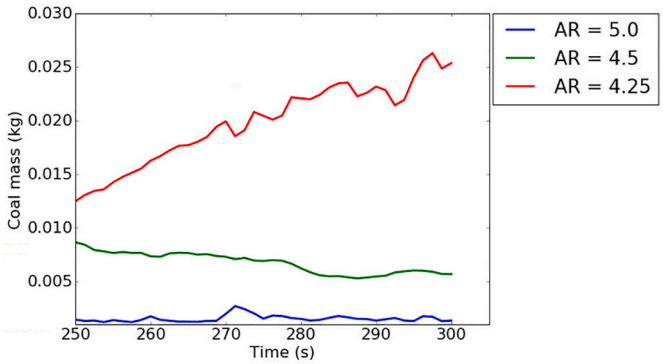

Fig. 10. Overall system coal mass (kg) vs. time (s) for AR velocities of 5.0, 4.5, and 4.25 m/s with an FR velocity of 2.5 m/s.

because of the significantly decreased amount of coal conversion happening in this case as compared to both the other cases.

O_2 in the reduced inventory cases was lower in the AR exit, which was because of the higher circulation rate and increased inventory in the AR compared to the base. Interestingly, O_2 in the FR was lower in the reduced inventory case despite the higher temperature, indicating that the equilibrium partial pressure for O_2 was not reached. The CO_2 mol fraction was also much larger in the AR cyclone exit for the reduced inventory cases as well compared to the base case, a result of the higher AR-FR circulation and higher amounts of unreacted coal. CO_2 exit mol fraction was still relatively low in the 150 kg case but was noticeably larger in the 100 kg case.

The simulated oxygen concentration versus equilibrium oxygen concentration in the FR is plotted in Fig. 7 for the base case and the reduced inventory cases with the equilibrium concentration based on

Table 14
Other values for base and various cases where fluidizing velocity is changed.

AR velocity (m/s)	FR velocity (m/s)	AR Temperature top, bottom (°C)	FR Temperature top, bottom (°C)	*X* AR cyclone	*X* FR cyclone	Change in *X*	O_2 mol fraction at cyclone exit AR, FR	CO_2 mol fraction at cyclone exit AR, FR
4.25	2.5	925, 919	933, 920	0.73	0.21	0.52	0.050, 0.009	2.0×10^{-3}, 0.17
4.5		931, 923	954, 939	0.77	0.27	0.50	0.058, 0.019	2.0×10^{-3}, 0.16
4.75		933, 924	961, 943	0.86	0.33	0.53	0.072, 0.028	1.8×10^{-3}, 0.17
5.0		**959, 929**	**968, 955**	**0.84**	**0.29**	**0.55**	**0.11, 0.045**	**1.1×10^{-5}, 0.14**
5.5		975, 935	977, 964	0.90	0.29	0.61	0.13, 0.053	4.4×10^{-4}, 0.14
5.0	2.0	970, 926	981, 964	0.86	0.19	0.61	0.13, 0.052	7.0×10^{-7}, 0.16
	4.0	934, 924	947, 935	0.85	0.39	0.67	0.069, 0.028	1.7×10^{-3}, 0.11

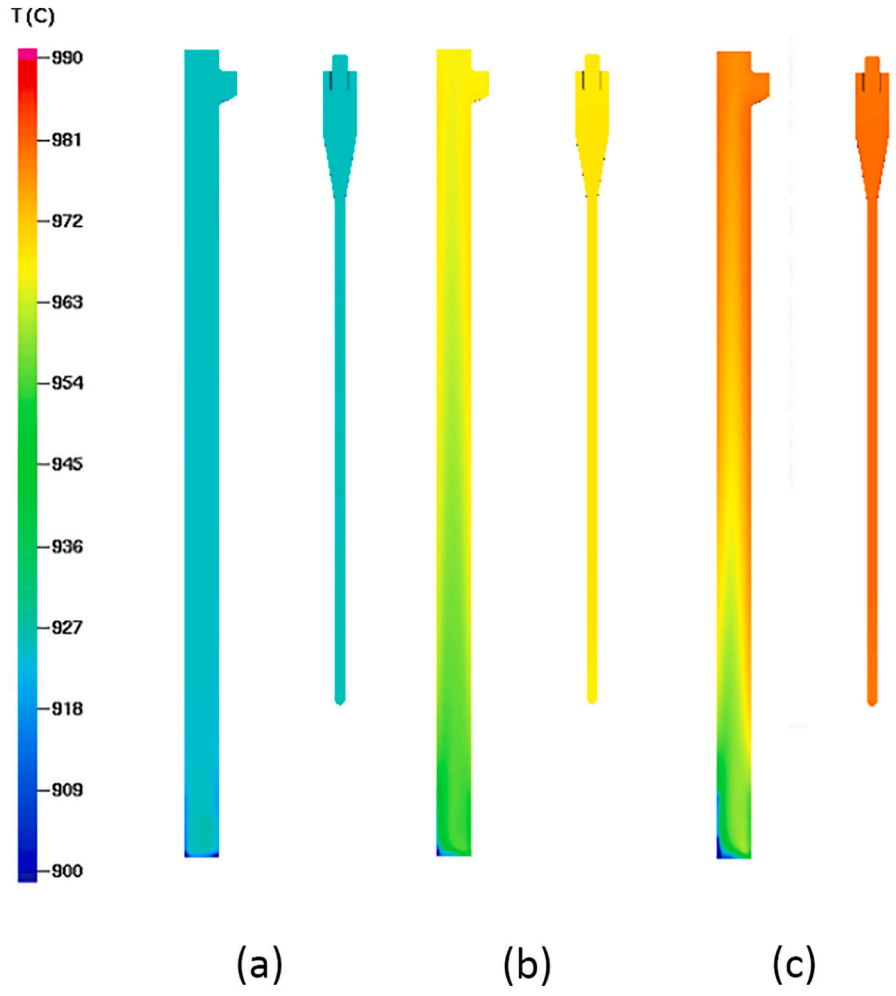

Fig. 11. Time-averaged fluid temperature for a cross-section of the AR for (a) AR = 4.25 m/s, (b) AR = 5.0 m/s, and (c) AR = 5.5 m/s cases. FR = 2.5 m/s.

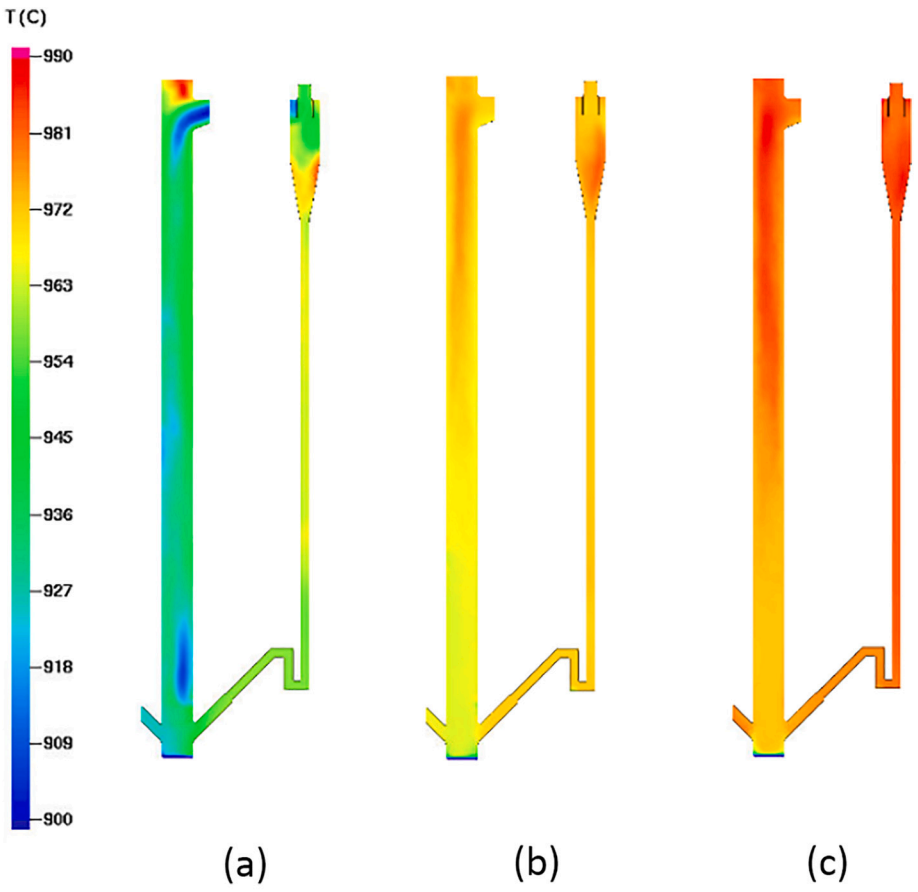

Fig. 12. Time-averaged fluid temperature for a cross-section of the FR for (a) AR = 4.25 m/s, (b) AR = 5.0, and (c) AR = 5.5 m/s cases. FR = 2.5 m/s.

local temperature. Despite the high temperatures in the top of the reactor potentially allowing for large amounts of oxygen to be released, the 150 kg inventory case did not reach equilibrium, suggesting that released oxygen was being quickly consumed by the fuel. The 100 kg case displayed similar behavior but also had significantly less O_2 present in the FR. This was most likely because this case had a larger amount of unreacted coal compared to the other two cases. The base case was much closer to equilibrium though it does not appear to be significantly limited by it.

Based on these results, 200 kg and 150 kg inventories appear to be acceptable for operation. The 100 kg resulted in a large build-up of unreacted coal and high pressures in the FR, resulting in blowback up the FRR dipleg and cyclone and is most likely untenable for actual operation. This could be possibly mitigated by increasing the copper oxide loading on the carrier to compensate for the lower amount of copper oxide content in the inventory or a decreased coal feed rate.

3.2.2. *Influence of Oxygen carrier Parameters*

These results compare the base case and changing the OC copper concentration from 20 to 30%, as well as the alternate, lower density oxygen carrier. As shown in Table 1, the density and particle size of the alternative carrier are dramatically different, and the copper content is 33%.

Table 11 lists hydrodynamic and mass parameters. Relative to the base case, the mass was about the same in the AR for the increased copper loading case and much higher in the alternate carrier case. This change in the alternate carrier case vs. the base case is similar to the change that was seen in the reduced inventory case. While the solids flow rate into the AR was similar to the base case, this was still a stark difference as the overall inventory in the alternate carrier case is only 90 kg as compared to 200 kg. The alternate carrier case had notably higher unreacted coal content than in the base case. Conversely, the increased copper loading case had less unreacted coal.

Table 12 lists the results for other parameters. The alternate carrier case had significantly less O_2 in the AR cyclone exit. The X of copper oxide in the AR cyclone, 0.71, was also low compared to the other cases. Likely this is a result of the higher residence time, resulting in more time for the carrier to oxidize.

Despite similar circulation rates, the base and alternate carrier cases had very different values for heat removal. This is primarily because there was significantly more carrier present in the AR for the alternate material case, resulting in better particle-wall heat transfer. The AR temperature was also a slightly higher for the alternate carrier case due to the overall lower inventory and less material to absorb released heat.

The AR oxygen concentrations were lowest in the alternate carrier case due to the fact that this carrier was in a more reduced state upon entering the reactor compared to the others, and the solids residence time in the AR was longer, thus providing more time for oxidation.

The oxygen concentration in the FR (Fig. 8) showed more significant variations. The increased copper loading case showed the highest level of oxygen in all parts of the FR. This is not unexpected, as this case also had the most copper oxide and the highest temperature allowing for a high equilibrium partial pressure of O_2. The alternate carrier case had slightly less O_2 in the FR than the base case. Again, since this case has less copper oxide content than the base case, this is reasonable.

Similar to the base case, the alternate carrier case did not reach the equilibrium partial pressure for O_2 (Fig. 9), likely because of the reduced overall copper oxide content in this case, similar to the reduced inventory case. Conversely, the higher copper oxide loading case overlaps with the equilibrium curve. In that case, if the reactor were hotter, even more O_2 would be released.

An alternate carrier with a similar copper oxide content to the base

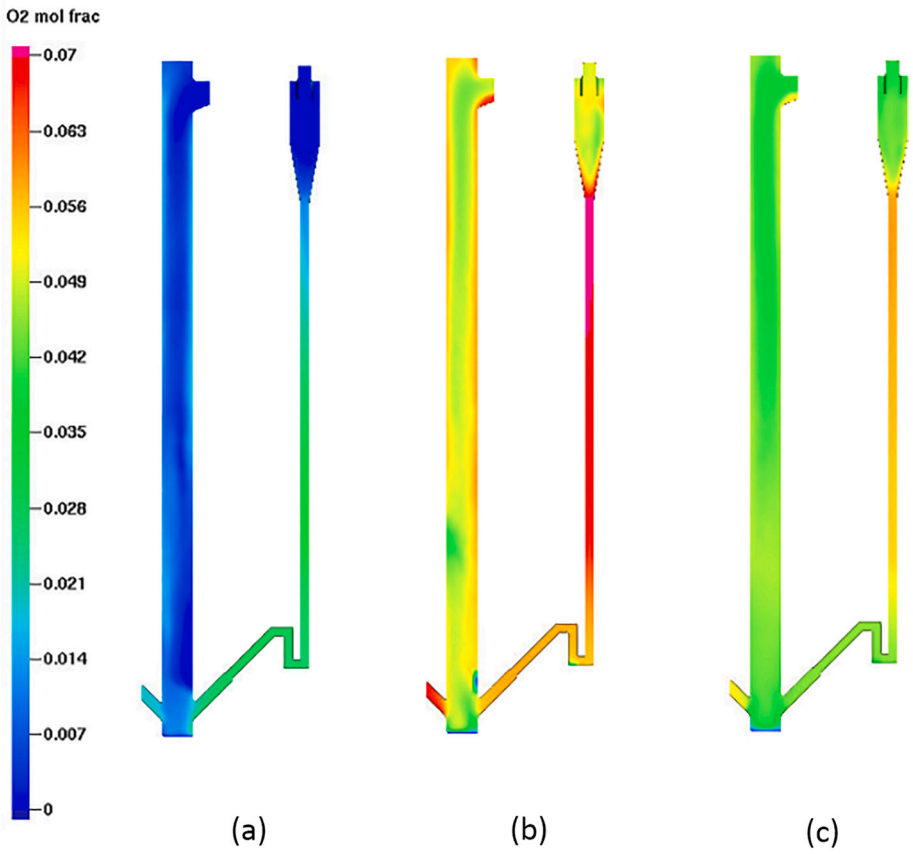

Fig. 13. Time-averaged O_2 mol fraction for a cross-section of the FR for (a) AR = 4.25, (b) AR = 5.0 m/s, and (c) AR = 5.5 m/s cases. FR = 2.5 m/s.

case appeared to work well and would likely be acceptable for operation. Similarly, increasing copper oxide content was beneficial with the exception of having a higher O_2 mol fraction in the FR cyclone exit, which is undesirable.

3.3. Influence of reactor velocity

Changing reactor superficial gas velocity has cascading effects on not only solids circulation rate and distribution but also on gas mol fractions, *X*, and the overall unreacted coal mass.

Table 13 lists hydrodynamic and mass parameters for different reactor velocities. The base case is highlighted in black. Decreasing AR velocity generally caused the inventory in the AR to increase substantially, even with relatively small changes. Coal mass in the system also increased significantly, especially at 4.25 m/s.

Decreasing the FR velocity from 2.5 to 2.0 m/s had little impact. AR mass was slightly lower, and the head of solids was backed-up in the FR-AR line, limiting the flow to the AR. Most likely, this was a result of the lower pressure in the FR. Increasing the velocity to 4.0 m/s significantly altered the inventory balance, with much more of the inventory being moved to the AR. This is consistent with the observation from the air reactor that higher velocities result in less reactor inventory. Notably, the coal mass in the system also increased in this case, possibly from the increased residence time of oxygen carrier in the AR, resulting in lower O_2 release in the FR.

Fig. 10 shows the transient coal mass in the FR for the changes in the AR velocity. As seen in this case, a decrease in AR velocity increases the mass of coal in the system, likely due to the decrease in the amount of oxygen carrier in the fuel reactor. The same was seen for the increase in the FR velocity, i.e., an increase in coal corresponding to the decrease in carrier in the fuel reactor.

The notably different cases were the higher AR flowrate case (5.5 m/s) and the two cases where FR flowrate was changed (2.0 and 4.0 m/s). When increasing the AR flowrate, the mass of O_2 in the AR increased, meaning that more oxygen carrier was oxidized before the reaction rate diminished, resulting in a higher *X* entering the FR. Changing the FR flowrate shifted the inventory balance significantly (Table 14) as well as the residence time. Decreasing the FR flowrate, increased the residence time in the FR, which resulted in a lower *X*. As the AR velocity was lowered, the O_2 mol fraction in the FR cyclone exit was also lower, with higher coal rates in the FR.

The temperature was notably lower for cases in which more inventory was in the AR, i.e., lower AR flowrates. Calculated heat removal in the AR also increases as the flow rate was lowered, spanning 52 kW to 120 kW. Correspondingly, the FR was at a lower temperature with lower temperatures in the AR.

CO_2 in the FR decreased when its superficial velocity increased because the mol fraction of steam was much higher due to the increased flow rate.

Increasing the AR flowrate resulted in higher temperatures and also increased O_2 mass in the reactor (Fig. 11). However, it should also be noted that the decreased AR velocity cases had significantly more mass inventory in the AR, resulting in more heat removal. As the FR temperature is closely tied to the AR temperature, these effects were also seen in the FR (Fig. 12). It should be noted that there are compounding effects of not only the AR temperature being lower but less coal combustion occurring in the 4.25 m/s case, ultimately resulting in a lower temperature.

In the FR, the high AR flowrates resulted in higher O_2 concentrations; however, in the 4.25 m/s case, the O_2 mol fraction was near zero in most of the reactor as a result of the low inventory (Fig. 13). This is likely the reason behind the increased coal amount over time as well.

Fig. 14 shows the oxygen concentrations compared to the equilibrium oxygen concentration. In the case of AR velocity at 4.25 m/s, the

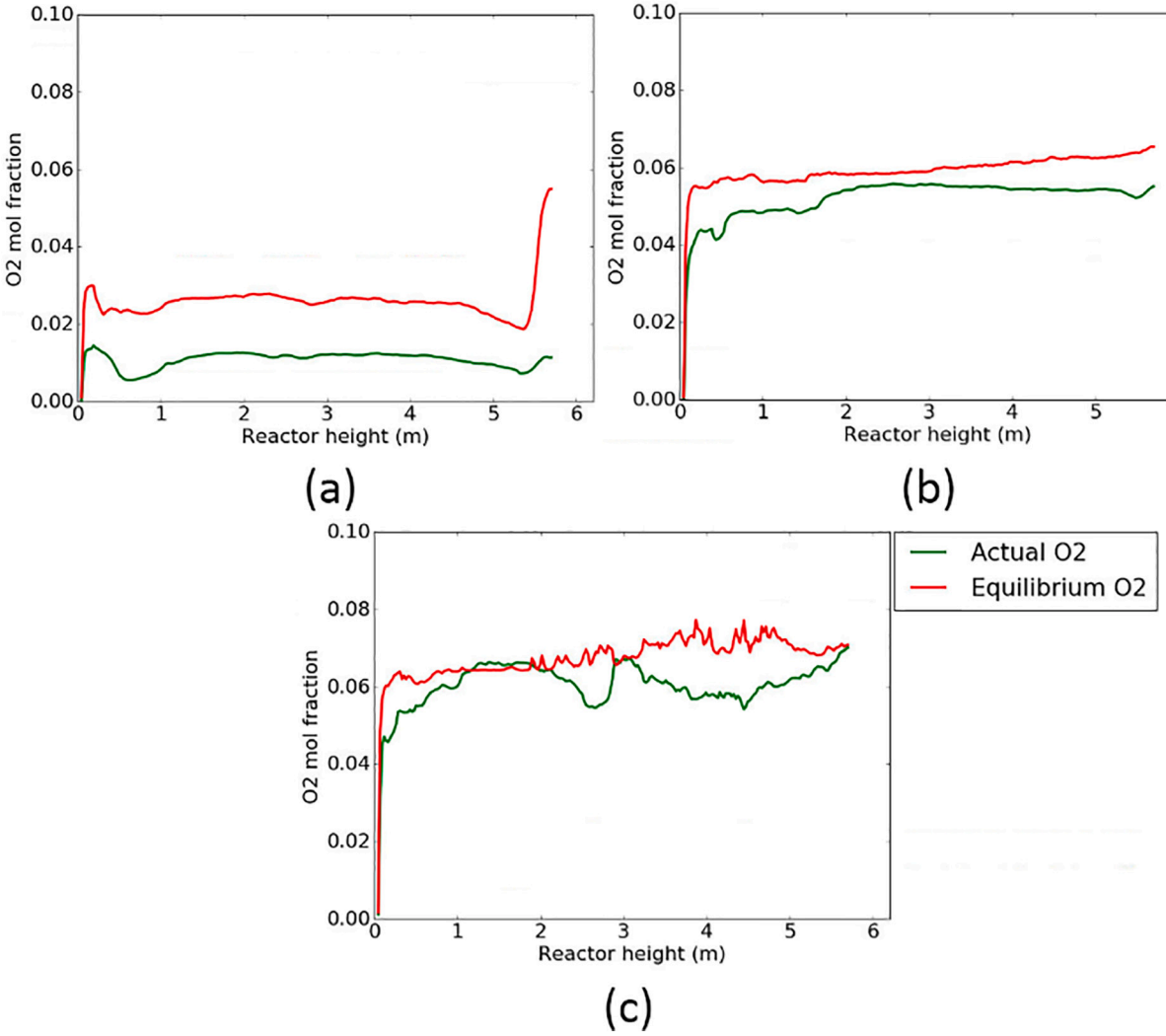

Fig. 14. O_2 mol fraction vs. FR reactor height (m) for (a) AR = 4.25 m/s, (b) AR = 5.0 m/s and (c) AR = 5.5 m/s.

FR oxygen concentration was not at equilibrium O_2 and was far below the base case of 5.0 m/s and the slightly higher 5.5 m/s case. There are several factors that could influence the low amount of O_2 in the 4.25 m/s case. The lower temperature in the FR in that case as compared to the base results in a slower reduction (O_2 release) reaction. Additionally, there is overall just less O_2 present in that case, as the superficial velocity of air into the AR is lower. Potentially the largest reason would be the excess of unreacted coal in that case as compared to the base case (20× higher).

Increasing the FR velocity increased the AR inventory. As was the case above, a higher AR inventory resulted in more heat removal, and the system, both the AR and the FR, were at lower temperatures. The O_2 mol fraction in the FR dropped as well, e.g., the concentration was noticeably low in the 4.0 m/s FR velocity case compared to the 2.5 and 2.0 m/s cases.

Reactor velocity was found to have a strong effect on inventory and can be used to control inventory balance if it is desirable to push mass into one reactor or another. The 4.25 m/s AR case was untenable, though, and did not provide enough O_2 to sustain coal combustion, and therefore is not recommended for actual operation.

4. Conclusions

A case-study of 3D simulations for CLOU was carried out using Barracuda-VR™, which explored changing fuel, oxygen carrier, and operating conditions. The results of the simluations can be applied generally to other chemical looping systems beyond the one studied. The results on coal particle size, oxygen distributions and availability, and the dependency between temperature and oxygen concentration are important contributions to operation.

Increasing the average coal particle size from 150 μm to 1000 μm showed no significant effect other than concentrating most of the coal particles into the bottom portion of the FR. In the base case, a large fraction of the coal oxidation occurred in the FR cyclone. It is noteworthy that the simulation did not predict a significant amount of coal entering the AR even when using a larger coal size. This indicates that larger coal could be used to prevent entrainment of coal into the cyclone without running the risk of transporting a significant amount to the AR, lowering the carbon capture efficiency.

For a given coal feed rate, sufficient oxygen must be transferred from the air reactor to combust the fuel in the fuel reactor. Whether that is achieved depends on coal feed rate, oxygen carrier circulation rate and inventory, oxygen carrier copper loading, and ΔX.

In the cases studied here, lowering the fuel input rate from 200 kW to 50 kW in increments of 50 kW resulted in a significant temperature drop in the overall system and low utilization of the oxygen carrier. The results suggest that a unit should be operated such that a high utilization of oxygen carrier is maintained for efficiency of the unit. However, if too much fuel is used, then the unit is no longer stable, insufficient oxygen is transferred, and unburned coal builds up.

Reducing system inventory from 200 kg to 150 kg and 100 kg predicted less O_2 in the FR. This was especially noticeable in the 100 kg case, which was unable to transport enough O_2 from the AR to FR to complete coal combustion. A compounded effect of less inventory was that the system was hotter, which further increased the difficulty in moving O_2 from AR to FR as this increased the equilibrium partial pressure and reduced oxidation driving force in the AR. Better performance for this case could be achieved with higher copper loading and potentially a slightly higher AR velocity, decreasing the AR inventory to input more O_2 into the fuel reactor. In the case of 100 kg, only approximately 40 kg of oxygen carrier was in the fuel reactor. The same result was seen in the velocity studies. At a AR velocity of 4.25 m/s, there was approximately 40 kg in the FR. In both cases the residence time in the FR was less than 30 s. This reduction of oxygen in the FR led to higher amounts of unburned coal.

Higher copper loadings, with the same amount of inventory, yielded the lowest amount of unreacted coal; unfortunately, this case also had an extremely large amount of unreacted O_2. The alternative carrier case, which had much lower inventory but higher copper oxide loading, was still successful—demonstrating that a different carrier type can be used effectively.

Changes to reactor velocity resulted in cascading effects through the simulations including the effects discussed above with FR inventory. Increasing the FR fluidizing velocity or decreasing the AR fluidizing velocity, both resulted in lower FR inventory. Correspondingly, higher inventories in the AR resulted in a lower temperature in the system and more heat removal. As a result, the fuel reactors had more coal in them due to less oxygen release as a result of less mass in the FR and changes in temperature.

For the three cases where coal was allowed to build up in the fuel reactor, 300 kW, 100 kg reduced inventory, and 4.25 m/s AR velocity, the system ultimately failed due to the unburned coal accumulation. Under these circumstances, the FR pressure increased, forcing inventory into the AR and restricting the flow of solids into the FR itself. In the 100 kg and 300 kW simulations, blowback was observed into the FRR dipleg and cyclone. Therefore, in actual operation, it is critical to maintain inventory in the FR and enough oxygen in the system to burn out the coal.

Important generalized findings for potential commercial CLOU units have been gained from the study. First, a larger coal size (1000 μm) appears to be acceptable and does not appreciably increase the amount of coal combusted in the AR. Second, special attention must be given to O_2 concentraton in both the AR and the FR. An AR velocity that is too low does not supply enough O_2 to the system to complete combustion. O_2 in the FR is also extremely important. A decrease in O_2 from operating conditions may result in unreacted coal building up in the system, perpetuating a failure state where the temperature continues to decrease in the FR from the lack of combustion, reducing the partial pressure of O_2 at equilibrium, further lowering the amount of combustion possible. O_2 should be maintained in the FR by ensuring a high enough AR velocity and a large enough supply of oxygen carrier inventory to handle the chosen coal feed rate.

Author statement

This statement certifies that all authors have seen and approved the final version of the manuscript being submitted. The article is the authors' original work, hasn't received prior publication and isn't under consideration for publication elsewhere.

Declaration of Competing Interest

None.

Acknowledgments

This material is based upon work supported by the U.S. Department of Energy under Award Number DE-FE0029160. The views and opinions of authors expressed herein do not necessarily state or reflect those of the United States Government or any agency thereof.

References

[1] A. Abad, I. Adánez-Rubio, P. Gayán, F. García-Labiano, L.F. de Diego, J. Adánez, Demonstration of chemical-looping with oxygen uncoupling (CLOU) process in a 1.5kW th continuously operating unit using a Cu-based oxygen-carrier, Int. J. Greenhouse Gas Control 6 (2012) 189–200, https://doi.org/10.1016/j.ijggc.2011.10.016.

[2] I. Adánez-Rubio, A. Abad, P. Gayán, L.F. de Diego, F. García-Labiano, J. Adánez, Performance of CLOU process in the combustion of different types of coal with CO2 capture, Int. J. Greenhouse Gas Control 12 (2013) 430–440, https://doi.org/10.1016/j.ijggc.2012.11.025.

[3] I. Adánez-Rubio, A. Abad, P. Gayán, L.F. De Diego, F. García-Labiano, J. Adánez, Biomass combustion with CO2 capture by chemical looping with oxygen uncoupling (CLOU), Fuel Process. Technol. 124 (2014) 104–114, https://doi.org/10.1016/j.fuproc.2014.02.019.

[4] J. Adánez, A. Abad, Chemical-looping combustion: Status and research needs, Proc. Combust. Inst. 37 (4) (2019) 4303–4317, https://doi.org/10.1016/j.proci.2018.09.002.

[5] M.J. Andrews, P.J. O'Rourke, The multiphase particle-in-cell (MP-PIC) method for dense particulate flows, Int. J. Multiphase Flow 22 (2) (1996) 379–402, https://doi.org/10.1016/0301-9322(95)00072-0.

[6] S. Banerjee, R. Agarwal, Transient reacting flow simulation of spouted fluidized bed for coal-direct chemical looping combustion with different Fe-based oxygen carriers, Appl. Energy 160 (2015) 552–560, https://doi.org/10.1016/j.apenergy.2015.10.013.

[7] R. Beetstra, M.A. van der Hoef, J.A.M. Kuipers, Numerical study of segregation using a new drag force correlation for polydisperse systems derived from lattice-Boltzmann simulations, Chem. Eng. Sci. 62 (1–2) (2007) 246–255, https://doi.org/10.1016/j.ces.2006.08.054.

[8] A. Chavda, A. Harichandan, Numerical analysis of bubble hydrodynamics in a steam reactor chemical looping reforming system, in: Lecture Notes in Mechanical Engineering, Pleiades Publishing, 2019, pp. 333–341, https://doi.org/10.1007/978-981-13-2697-4_37.

[9] X. Chen, J. Ma, H. Zhao, CPFD Simulation and Optimization for a 50 kW th Dual Circulating Fluidized Bed Reactor for Chemical Looping Combustion of coal. September, 24–27, 2018.

[10] C.K. Clayton, H.Y. Sohn, K.J. Whitty, Oxidation kinetics of Cu2O in oxygen carriers for chemical looping with oxygen uncoupling, Ind. Eng. Chem. Res. 53 (8) (2014) 2976–2986, https://doi.org/10.1021/ie402495a.

[11] J. Dai, K. Whitty, Effects of Coal Ash on CuO as Oxygen Carrier for Chemical Looping with Oxygen Uncoupling (CLOU). September, 24–27, 2018.

[12] J.K. Dansie, A.H. Sahir, M.A. Hamilton, J.S. Lighty, An investigation of steam production in chemical-looping combustion (CLC) and chemical-looping with oxygen uncoupling (CLOU) for solid fuels, Chem. Eng. Res. Des. 94 (2015) 12–17, https://doi.org/10.1016/j.cherd.2014.11.011.

[13] E.M. Eyring, G. Konya, J.S. Lighty, A.H. Sahir, A.F. Sarofim, K. Whitty, Chemical looping with copper oxide as carrier and coal as fuel chemical looping-an alternative concept for efficient and clean use of fossil resources La Boucle Chimique-Un concept alternatif pour un usage propre et efficace des ressources fossiles NOTATION symbols, Oil Gas Sci. Technol. Rev. IFP Energies Nouvelles 66 (2) (2011) 209–221, https://doi.org/10.2516/ogst/2010028.

[14] Z. Hamidouche, X. Ku, J. Lin, J. Wang, Numerical simulation of a chemical looping combustion of biomass: hydrodynamic investigation, Fuel Process. Technol. 207 (2020) 106486, https://doi.org/10.1016/j.fuproc.2020.106486.

[15] Z. Hamidouche, E. Masi, P. Fede, O. Simonin, K. Mayer, S. Penthor, Unsteady three-dimensional theoretical model and numerical simulation of a 120-kW chemical looping combustion pilot plant, Chem. Eng. Sci. 193 (2019) 102–119, https://doi.org/10.1016/j.ces.2018.08.032.

[16] M.A. Hamilton, Z. Reinking, K.J. Whitty, J.S. Lighty, Particle fluid dynamic code validation with hydrodynamics, in: Particle Technology Forum 2017 - Core Programming Area at the 2017 AIChE Annual Meeting, 2017-Octob, 2017.

[17] Matthew A. Hamilton, K.J. Whitty, J.A.S. Lighty, Incorporating oxygen uncoupling kinetics into computational fluid dynamic simulations of a chemical looping system, Energy Technol. 4 (10) (2016) 1237–1246, https://doi.org/10.1002/ente.201600031.

[18] T.M. Ismail, L. Ding, K. Ramzy, M. Abd El-Salam, Numerical and experimental analysis for simulating fuel reactor in chemical looping combustor system, Int. J. Coal Sci. Technol. (2020) 1–9, https://doi.org/10.1007/s40789-020-00351-y.

[19] K. Jayaraman, I. Gokalp, E. Bonifaci, N. Merlo, Kinetics of steam and CO2 gasification of high ash coal-char produced under various heating rates, Fuel 154 (2015) 370–379, https://doi.org/10.1016/j.fuel.2015.02.091.

[20] Z. Li, H. Xu, W. Yang, A. Zhou, M. Xu, CFD simulation of a fluidized bed reactor for biomass chemical looping gasification with continuous feedstock, Energy Convers. Manag. 201 (2019) 112143, https://doi.org/10.1016/j.enconman.2019.112143.

[21] A. Lyngfelt, Chemical-looping combustion of solid fuels-status of development, Appl. Energy 113 (2014).

[22] T. Mattisson, Materials for chemical-looping with oxygen uncoupling, ISRN Chem. Eng. 2013 (1) (2013) 1–19, https://doi.org/10.1155/2013/526375.
[23] T. Mattisson, A. Lyngfelt, H. Leion, Chemical-looping with oxygen uncoupling for combustion of solid fuels, Energy Procedia 3 (2009) 11–19, https://doi.org/10.1016/j.ijggc.2008.06.002.
[24] J. May, F. Alobaid, P. Ohlemüller, A. Stroh, J. Ströhle, B. Epple, Reactive two–fluid model for chemical–looping combustion – simulation of fuel and air reactors, Int. J. Greenhouse Gas Control 76 (2018) 175–192, https://doi.org/10.1016/j.ijggc.2018.06.023.
[25] K.M. Merrett, K.J. Whitty, Conversion of Coal in a Fluidized Bed Chemical Looping Combustion Reactor with and without Oxygen Uncoupling, 2019, https://doi.org/10.1021/acs.energyfuels.8b03581.
[26] P.J. O'Rourke, D.M. Snider, An improved collision damping time for MP-PIC calculations of dense particle flows with applications to polydisperse sedimenting beds and colliding particle jets, Chem. Eng. Sci. 65 (22) (2010) 6014–6028, https://doi.org/10.1016/j.ces.2010.08.032.
[27] J.M. Parker, CFD model for the simulation of chemical looping combustion, Powder Technol. (2014) 1–7, https://doi.org/10.1016/j.powtec.2014.01.027.
[28] A. Passalacqua, R.O. Fox, Advanced continuum modelling of gas-particle flows beyond the hydrodynamic limit, Appl. Math. Model. 35 (4) (2011) 1616–1627, https://doi.org/10.1016/j.apm.2010.09.038.
[29] Z. Reinking, H.-S. Shim, K.J. Whitty, J.S. Lighty, Computational simulation of a 100 kW dual circulating fluidized bed reactor processing coal by chemical looping with oxygen uncoupling, Int. J. Greenhouse Gas Control 90 (2019) 102795, https://doi.org/10.1016/j.ijggc.2019.102795.
[30] A.H. Sahir, H.Y. Sohn, H. Leion, J.S. Lighty, Rate analysis of chemical-looping with oxygen uncoupling (CLOU) for solid fuels, Energy Fuel 26 (7) (2012) 4395–4404, https://doi.org/10.1021/ef300452p.
[31] J. Smagorinsky, J. Smagorinsky, General Circulation Experiments with the Primitive Equations, 1963, https://doi.org/10.1175/1520-0493(1963)091<0099:GCEWTP>2.3.CO;2.
[32] Dale M. Snider, An incompressible three-dimensional multiphase particle-in-cell model for dense particle flows, J. Comput. Phys. 170 (2) (2001) 523–549, https://doi.org/10.1006/jcph.2001.6747.
[33] Dale M. Snider, S.M. Clark, P.J. O'Rourke, Eulerian-Lagrangian method for three-dimensional thermal reacting flow with application to coal gasifiers, Chem. Eng. Sci. 66 (6) (2011) 1285–1295, https://doi.org/10.1016/j.ces.2010.12.042.
[34] Liu Wang, Zhang Zhang, Jin, Numerical investigation of solid-fueled chemical looping combustion process utilizing char for carbon capture, Processes 7 (9) (2019) 603, https://doi.org/10.3390/pr7090603.
[35] W.-C. Yang, Handbook of fluidization and fluid-particle systems, China Particuol. (2003), https://doi.org/10.1016/s1672-2515(07)60126-2.